ISSN 0018-151X, High Temperature, 2023, Vol. 61, No. 3, pp. 350–357. © Pleiades Publishing, Ltd., 2023.
Russian Text © The Author(s), 2023, published in Teplofizika Vysokikh Temperatur, 2023, Vol. 61, No. 3, pp. 382–390.

THERMOPHYSICAL PROPERTIES OF MATERIALS

First-Principal Study of Proton Transfer in Metal Oxide Perovskite

A. E. Galashev[a, b, *]

[a] *Institute of High-Temperature Electrochemistry, Ural Branch, Russian Academy of Sciences, Yekaterinburg, Russia*
[b] *Ural Federal University named after First President of Russia B.N. Yeltsin, Yekaterinburg, Russia*
**e-mail: galashev@ihte.uran.ru*

Received June 11, 2022; revised November 1, 2022; accepted December 6, 2022

Abstract—The mechanism of proton conduction of defect-free perovskite $LaScO_3$ was investigated by *ab initio* molecular dynamics. The effects of the initial location and speed of a proton, the electric field, and the temperature of the system on the behavior of a proton in metal oxides of the perovskite type are considered. It is shown that the temperature of the system is the main factor affecting the speed of proton movement. The Arrhenius temperature behavior of proton conduction is found. In the absence of oxygen vacancies, the direction of proton movement in a crystal with a perovskite structure is determined by its interaction with lattice phonons; i.e., proton migration through metal-oxide perovskite has a polaronic character. Better understanding of the nature of proton migration along the perfect perovskite is one of the ways to improve the characteristics of clean energy devices.

DOI: 10.1134/S0018151X23030112

INTRODUCTION

One of the most important applications of proton-conducting electrolytes is their use in solid oxide fuel cells (SOFC) [1]. When hydrogen is the fuel for these devices, they use almost 100% of it and do not pollute the atmosphere with combustion products that change the geospheric thermal balance [2]. The high efficiency of electricity generation puts SOFC among a number of candidates for future energy sources. However, due to the high operating temperatures (800–1000°C), it is difficult to start these devices quickly. Reaching operating temperatures below 600°C is important for expanding the possibilities of using SOFC and reducing its cost. In addition to natural gas and hydrogen, the high operating temperature of SOFC allows them to use other types of fuel. In particular, a technology for converting waste into energy has been developed on the basis of SOFC [3, 4]. However, the chemical stability of such devices is not yet satisfactory [5, 6].

Another application of SOFC is its use as an electrolyzer for splitting water and producing hydrogen with the cost of electricity. SOFC operating in this mode is defined as a solid oxide electrolysis cell. It is expected that due to their ability to use and produce hydrogen, SOFC will play an important role in the transition to hydrogen energy [7].

There is a field of application of proton-conducting electrolytes at lower temperatures. In particular, they can be used for lithium-ion batteries (LIB). Among solid electrolytes, some glasses and crystalline compounds are considered, including doped $LaScO_3$, where Li^+ ions diffuse through vacancies. The use of solid electrolytes for metal-ion batteries has a number of advantages over the use of liquid electrolytes. Solid electrolytes can provide fire safety and help avoid electrolyte leakage. Their use will increase the energy density and lead to a longer battery life due to increased viability during cycling. The Coulomb efficiency will increase, a wider window of electrochemical stability will appear, and the operating temperature range will expand. However, this can be achieved using a solid electrolyte with high ionic conductivity.

Metal-oxide perovskites have the ABO_3 structure shown in Fig. 1a, in which densely packed layers of AO_3 are stacked one above the other through ordered layers of B and O ions. In this case, B cations occupy octahedral voids (Fig. 1b), surrounded by oxygen located at the vertices of octahedra (Fig. 1c). In the $LaScO_3$ compound, the A ion is La, and the B ion is Sc.

In the group of oxides, high conductivity ($>10^{-3}$ S cm^{-1}) at room temperature have Li–La–Ti–O

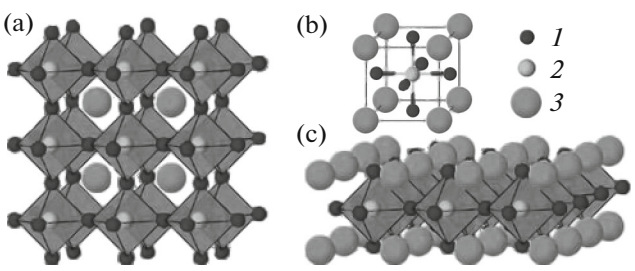

Fig. 1. (a) View of ABO_3 structure of metal-oxide perovskite; (b) ion B (*2*) surrounded by ions O (*3*) and A (*1*); (c) packing of layers in ABO_3 perovskite.

perovskite [8]. To obtain it, high temperatures are required (>1000°C). The main disadvantage of perovskite is the reduction of the Ti^{4+} element to Ti^{3+} during the electrochemical process, which creates undesirable electron conductivity [9]. In this perovskite structure, ionic conductivity is achieved by introducing lithium vacancies in the A position [10]. However, in practice, cases are more common when lithium fills the internodes of perovskite.

$LaScO_3$ perovskite is considered as the initial structure of a solid electrolyte suitable for use in LIB [11]. It has been shown that the B-position cation Sc^{3+} has a higher resistance to electrochemical reduction than Ti^{4+} [12]. When the low-valence Li^+ cation partially replaces the high-valence La^{3+} cation, structural defects are formed. Defect formation is associated with charge compensation produced by interstitial lithium atoms. After the introduction of lithium into $LaScO_3$, for to obtain the compound $(Li_xLa_{1-x/3})ScO_3$, further modification is carried out to improve its ionic conductivity by introducing additional structural defects. Ce^{4+} and Zr^{4+} or Nb^{5+} can be selected as an alloying impurity to achieve the highest conductivity [8]. They partially replace the A or B positions in $(Li_xLa_{1-x/3})ScO_3$. The behavior of H^+ and Li^+ cations in defect-free perovskite $LaScO_3$ remains poorly studied.

Perovskites are widely used in the manufacture of solar cells, the efficiency of which reaches 25.7% [13]. An increase in efficiency by reducing losses can be achieved by passivating defects at the grain boundaries and on the surface of the perovskite film [14]. Defects negatively affect the performance of the solar battery.

The aim of this article was to study the influence of temperature, electric field, initial location and speed of a proton in defect-free oxide perovskite $LaScO_3$.

SOLID OXIDE FUEL CELL BASED ON HYDROGEN

Hydrogen is a very attractive fuel, but in contrast to, e.g., coal and wind, it is difficult to access. This is because there is hardly any free hydrogen in our environment. The most available sources of hydrogen today are water and natural gas. The attractiveness of hydrogen as a fuel lies not only in its high energy intensity; hydrogen is an energy source that does not pollute the environment when releasing energy. The conversion of the chemical energy of hydrogen into electric energy is carried out using a fuel cell.

A fuel cell is a device that efficiently generates heat and direct current as a result of an electrochemical reaction. Hydrogen-rich fuel or pure hydrogen is used to carry out the reaction. The fuel cell is similar in principle to a battery, but it also has fundamental differences from it. Structurally, the fuel cell is represented by a cathode, an anode and an electrolyte membrane (Fig. 2). Unlike a battery, a hydrogen fuel cell does not accumulate electric energy, does not require electric charging to resume operation, and does not discharge. The element generates electricity as long as there is a supply of air and fuel.

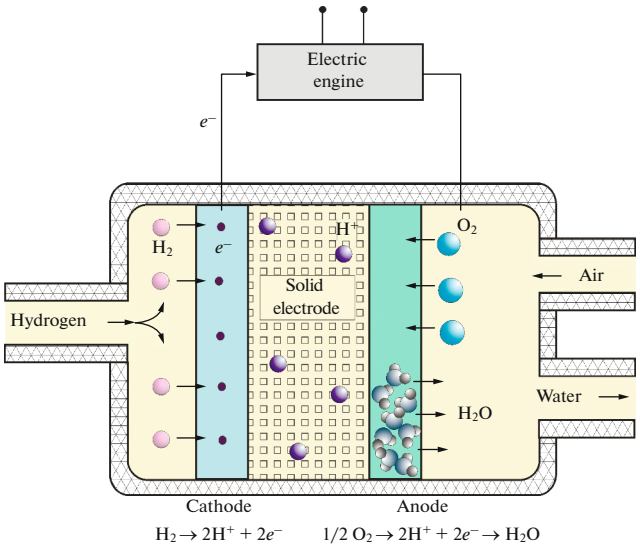

Fig. 2. Schematic diagram of hydrogen fuel cell.

The problem of hydrogen storage is one of the main obstacles to its use. Under normal conditions, hydrogen occupies an extremely large space. There are two ways to make the hydrogen storage more compact. To do this, it is necessary to use liquefied hydrogen or compressed gaseous hydrogen. However, hydrogen becomes liquid at a very low temperature, just a few degrees above absolute zero. In addition, too much energy is required to liquefy hydrogen, namely, about 40% of the electric energy generated using it. At the same time, a huge amount of CO_2 is emitted into the atmosphere. The second method of storing hydrogen is more acceptable. For wider consumption, including in cars, hydrogen gas is compressed to a pressure of approximately 60–70 MPa. The multistage process of hydrogen compression requires a cost of 10–15% of the electricity generated using the resulting compressed hydrogen.

The advantage of hydrogen over traditional automotive fuel (gasoline) is to reduce the danger associated with fuel leakage and the presence of a spark. In the event of a leak, hydrogen will simply escape into the atmosphere, and hydrogen gas is nontoxic. At the same time, hydrogen has an extremely low ignition energy (almost 20 times lower than that of gasoline). However, leakage of hydrogen into a room with a high oxygen content is not exempt from fire hazard. The efficiency of fuel cells is approximately 50–60%, and when combined with hybrid gas turbine systems, the efficiency can increase up to 70%.

Electrolyte membranes are of paramount importance for the continuous and efficient functioning of the entire fuel cell. Their low porosity is one of the prerequisites to prevent the transfer of fuel into them and

loss of voltage between the anode and cathode. At the same time, the solid electrolyte must have a high proton conductivity to ensure proton transfer between the electrodes. It also requires good chemical and thermal stability in the operating conditions of fuel cells. Given the above, the study of the nature of proton movement through a solid electrolyte seems an extremely important problem.

COMPUTATIONAL MODEL

Molecular dynamic (MD) *ab initio* calculations based on density functional theory using the local electron density (LED) approximation were performed using the SIESTA software package. The calculation of the exchange-correlation functional was based on the Purdue–Burke–Ernserhof formalism [15]. The supercell consisted of 16 La atoms, 16 Sc atoms and 48 oxygen atoms. Periodic Born–Karman boundary conditions were used in the calculations. The parameters of the initial lattice were determined as $a = 11.6$ Å, $b = 8.1$ Å, $c = 11.3$ Å, $\alpha = \beta = \gamma = 90°$, and the volume of the created system was 1068.8 Å^3.

SIESTA is a software based on pseudopotentials, so GGA pseudopotentials were taken from the SIESTA database. Ultrasoft pseudopotentials were used in the calculations [16]. These pseudopotentials were optimized by minimizing the difference in the calculation results of various electronic configurations obtained in the pseudopotentials approximation and taking into account the energy of all electrons.

The Hamiltonian for the considered system of many bodies includes the kinetic energy operator for electrons, the potential acting on electrons from the nucleus, the electron-electron interaction, the kinetic energy operator for the nucleus, and the internuclear interaction. SIESTA implements strictly localized numerical atomic orbitals. In other words, the Schrödinger equation for an isolated atom is solved on the basis of potential confinement, which makes the orbital zero beyond a given circumcision radius. Using such an approximation reduces the number of basic functions used, which leads to a very high efficiency of the method, when the memory and processor time used are significantly reduced. Simple physical interpretation (the ability to analyze the population and density of the state) and the achievement of high accuracy are also the advantages of this approach. However, choosing a good basis in SIESTA and a way to extend it (to improve convergence) is not a trivial problem.

Three important parts of the SIESTA mechanism can be distinguished: pseudopotentials, the basis, and the functioning of the *k*-grids.

The basis set was formed using the data in [16]. The DZP option was used, which ensures the cardinality of the basic set (the circumcision radius, the main quantum number of the shell, and the angular momentum of the basic orbitals of this shell). At the same time, SIESTA is guided by internal heuristics to decide which orbitals are really needed. Using this option involves finding an equilibrium configuration by performing structural relaxation using conjugate gradients for the selected dual basis. Calculations using linear density approximation (LDA) were performed using a code with a direct diagonalization of the Hamilton matrix. The basis of pseudoatomic orbitals was a local basis with a simple construction of the radial function $R_{nl\zeta}(r)$ multiplied by the corresponding spherical harmonic. The value of the radial function was determined by the principal quantum number n, the orbital angular momentum l, and the number of functions per l channel ζ given in terms of the spherical function.

A not too dense, and therefore not very "expensive" for SIESTA, grid was used, which nevertheless provided acceptable convergence. The Brillouin zone was determined by $10 \times 10 \times 1$ k-points, which were generated using the Monkhorst–Pack algorithm [17]. The density of the three-dimensional grid used to calculate the electron density was set using a cut-off energy equal to 400 Ry (Ry is the Rydberg constant used in formulas for calculating the energy levels and radiation frequencies of atoms, Ry = 2.179872×10^{-18} J).

Integration of the equations of motion in the ab initio implementation of molecular dynamics was carried out by the Verle method with a time step of 1 fs. Geometric optimization was performed before each MD ab initio calculation. The dynamic relaxation of the atoms continued until the change in the total energy of the system became less than 10^{-4} eV. Then, after relaxation, a proton was placed in the system, which occupied different positions:

(a) in the plane of the Sc octahedron between the oxygen atoms at point 1;

(b) in the plane of the Sc octahedron near the oxygen atom at point 2;

(c) in the plane of La atoms with localization near the oxygen atom at point 3.

MD calculations based on first principles for systems containing a proton were performed with an initial proton speed that varied from $v_0 = 0$ to 0.37418×10^5 m/s. An electric field acted on a proton, the intensity vector of which lay in the xz plane. The directions of this vector changed, and the voltage value changed from E 0 to 3.5×10^{10} V/m. Nine calculations were carried out with a length of approximately 1000 time steps in the temperature range from 153 to 1100 K. The last temperature value was close to the operating temperature of SOFC using $LaScO_3$-based compounds as an electrolyte. Data on the temperature, the applied electric field, the initial speed of a proton and its initial location are presented in the Table 1. To determine the time points at which a proton jumped from one oxygen atom to another, an appropriate algorithm has been developed, the code of which is implemented in Python 3.8. This algorithm is based on tracking changes in the potential energy of a proton. The peaks

Table 1. Characteristics of initial data and calculated temperature for series of nine *ab initio* molecular dynamic calculations

Calculation no.	1	2	3	4	5	6	7	8	9
E_x, 10^{10} V/m	0.5	0.5	0	1.5	1.5	1.5	3.5	3.5	3.5
E_y, 10^{10} V/m	0	0	0	0	0	0	0	0	0
E_z, 10^{10} V/m	0.5	0.5	0	1.5	1.5	1.5	3.5	3.5	3.5
E, 10^{10} V/m	0.7071	0.7071	0	2.1213	2.1213	2.1213	4.9497	4.9497	4.9497
v_{0x}, 10^5 m/s	0.1058	0.2645	0.1058	0.2645	0.1058	0.2645	0	0	0
v_{0y}, 10^5 m/s	0	0	0	0	0	0	0	0	0
v_{0z}, 10^5 m/s	0	0.2645	0	0.2645	0.1058	0.2645	0	0	0
v_0, 10^5 m/s	0.1058	0.3741	0.1058	0.3741	0.1496	0.3741	0	0	0
Initial localization of proton*	1 (0.44, 0.75, 0.23)	1 (0.44, 0.75, 0.23)	1 (0.44, 0.75, 0.23)	2 (0.56, 0.75, 0.23)	3 (0.33, 0.75, 0.94)	3 (0.33, 0.75, 0.94))	3 (0.33, 0.75, 0.94)	3 (0.33, 0.75, 0.94)	3 (0.33, 0.75, 0.94)
T, K	684.78	848.31	682.05	904.31	134.91	255.00	153.43	668.80	1099.17

* The coordinates of a proton's initial locations in nm are given in parentheses.

on this dependence reflect the virtual settled positions of a proton, and the time interval between these peaks determines the time of its transition from one oxygen atom to another.

The diffusion coefficient D of a proton in metal oxide perovskite was calculated from the time dependence of the mean square of its displacement. The coefficient D can be expressed in terms of proton conductivity σ using the Nernst–Einstein equation

$$D = \frac{\sigma kT}{e^2 C_{\mathrm{H}}},$$

where k is the Boltzmann constant, T is the absolute temperature, e is elementary charge, and C_{H} is a proton concentration.

The activation energy was determined by the equation

$$\sigma = \sigma_0 \exp(-E_a/kT),$$

where σ_0 is the pre-exponential factor; E_a is the activation energy calculated from the slope of the linear dependence lnσ(1000/T).

RESULTS

Figure 3 shows the horizontal projections of the $LaScO_3$ crystal configurations corresponding to the moment of time 1 ps. In experiment 1, a constant electric field with a strength E = 0.7071 × 10^{10} V/m acted on a proton; experiment 3 was carried out in the absence of an electric field. In the presence of the field, the proton trajectory was enclosed in a more limited area of space than in its absence. It is noteworthy that most of the path a proton passed not in the direction determined by the intensity of the electric field, but in the direction forming a certain angle with the direction of the vector **E**. In both cases, the ion tra-

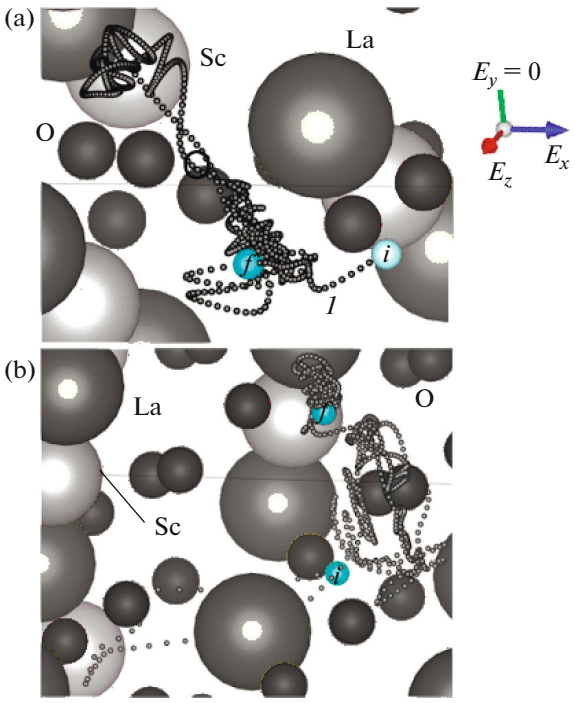

Fig. 3. Horizontal projections of $LaScO_3$ crystal configurations corresponding to time 1 ps: (a) in presence of electric field with strength of E = 0.7071 × 10^{10} V/m; (b) without electric field; *1*, proton trajectories for specified time interval; *i* and *f*, beginning and end of trajectory, respectively.

jectory turned out to be quite confusing. It could fall into the vicinity of another (different from the original) oxygen atom and stay there for a while. It could also converge with neighboring La and Sc atoms, which were not initially adjacent to it. In addition, a proton could not only move away from its original location, but also approach it again, moving in the direction opposite to the direction of the path already traveled. Thus, the electric field did not significantly affect the choice of the preferred direction of proton movement in the $LaScO_3$ crystal. Most likely, the location of its virtual location was determined by the attraction of a proton to any of the oxygen atoms closest to it.

The temperature dependence of the potential energy of $LaScO_3$ perovskite was not monotonous (Fig. 4). Sharp changes in the energy U in a small temperature range were observed at temperatures $T < 153$ K and in the range 668 K $\le T \le$ 685 K. In this temperature range, the highest energy U corresponded to the state with the highest value of the electric field, and the lowest energy appeared when the field was absent. The highest energy U in the entire temperature range under consideration was observed at $T = 1099$ K. This state was also obtained at the maximum of the electric field strength.

The behavior of a proton in the system significantly depended on the temperature of the perovskite. It is safe to say that there were no jumps of a protons at temperatures below 400 K; a proton oscillated around the oxygen atom, near which it was originally located. In the temperature range of 600–800 K, random jumps of a proton between oxygen atoms occurred. However, such jumps were quite rare. Most proton jumps were observed at temperatures above 800 K, when a proton had sufficient speed to overcome the potential barrier.

Observation of the behavior of a proton in a perovskite system in the temperature range of 680–850 K made it possible to identify the time interval during which proton made a jump to a neighboring oxygen atom or to another place of temporary localization.

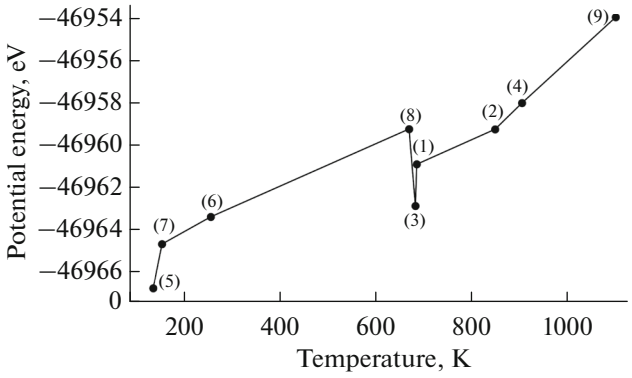

Fig. 4. Dependence of potential energy on temperature for calculated states of $LaScO_3$ perovskite; numerals, calculation nos. from Table 1.

In the time sweep of the potential energy, such an interval was always between the local extremes of the function $U(t)$. Figure 5 shows the functions $U(t)$ obtained in calculations 1–3 defined in Table 1. The time intervals during which proton jumped to a new settled position are highlighted in the figure with shaded stripes. In all cases, the duration of the jump interval did not exceed 100 fs, i.e., 100 time steps. Obviously, during such a period of time, a proton completely "forgot" the initial direction of its speed. The further speed of a proton was determined by the interatomic interaction, temperature, and partly by the direction of the electric field strength. The electric field did not completely determine the direction of motion of a proton, but it affected the instantaneous values of the potential energy: the larger the electric field, the greater the fluctuations of the $U(t)$ function. Comparison of Figs. 5a and 5b shows that the frequency of proton jumps could be influenced by the direction and magnitude of its initial speed. In particular, with a higher value of the speed, the time intervals between proton jumps increased. At the same time, comparison of Figs. 5a and 5c shows that the number of proton jumps in the presence of an electric field might not increase but, on the contrary, decreased.

Figure 6 shows the types of possible proton jumps in the $LaScO_3$ perovskite. The directions of the proton movement are shown by light segments connecting light circles (proton designations). In case I, a proton changes its position, moving from an oxygen atom belonging to one octahedron to an oxygen atom belonging to another octahedron, and a transition occurs between the La atoms. In case II, a proton, bypassing only one La atom, passes from one oxygen atom to another along the edge of the octahedron, and both oxygen atoms belong to the same octahedron. In

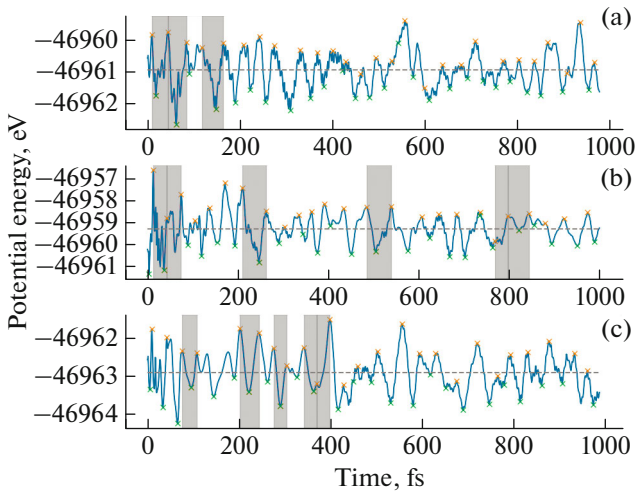

Fig. 5. Change in potential energy of perovskite system over time in calculations 1 (a), 2 (b), and 3 (c); shaded bands show periods of proton jumps between oxygen atoms; dashed line shows average potential energy.

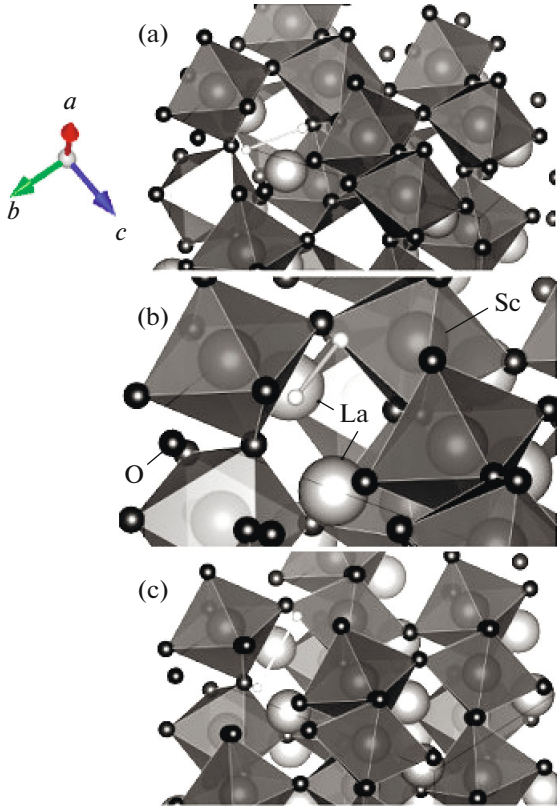

Fig. 6. Types of proton jumps in perovskite I (a), II (b), III and IV (c).

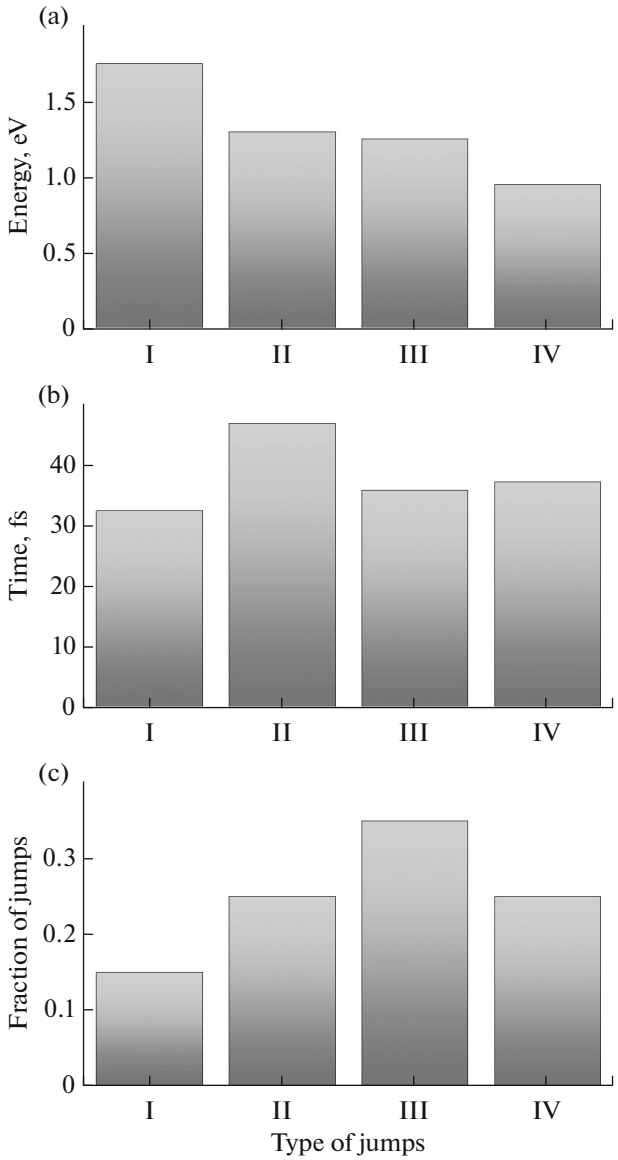

Fig. 7. Parameters for performing various types of proton jumps: (a) average height of energy barrier, (b) average time of jump, and (c) fraction of jumps of certain type from all jumps.

cases III and IV, a proton also passes through one La atom, but the oxygen atoms between which it moves are separated by an octahedron; i.e., together they belong to three neighboring octahedra. The forward and reverse paths of a proton in these cases are not equivalent due to the difference in the atomic environment. Therefore, we consider them separately, assuming that case III corresponds to a direct transition; i.e., a proton entering the plane of the octahedron, and case IV corresponds to the reverse transition.

Figure 7 shows the characteristics of proton jumps classified according to the four types defined above. Jumps of the type I can be characterized as proton migration in the lanthanum plane (the plane between octahedra). The jumps of type II occur on the scandium plane (in the plane of octahedra). Jumps of the type III involve the movement of a proton from the lanthanum plane to the scandium plane (transition to the octahedron plane). The type IV transition expresses a proton exit from the scandium plane and its return to the lanthanum plane.

Jumps of the first type are characterized by the highest energy barrier height, the shortest jump time (since in this case a proton acquires the greatest kinetic energy); and the number of jumps of this type is minimal. To make a jump of the second type, a proton also needs to acquire sufficiently large kinetic energy to overcome the second largest energy barrier. In this case, the jump time is the longest. The number of such jumps is a quarter of all jumps performed. The barrier for making jumps of the third type is somewhat less than for jumps of the second type, and the execution time of such jumps is noticeably less than for jumps of the second type, but somewhat longer than for jumps of the first type. The proportion of jumps of the third type turns out to be the largest. Jumps of the fourth type are characterized by the smallest energy barrier and take a little longer than jumps of the third type. The number of such jumps, as well as jumps of the second type, is a quarter of all jumps.

A proton migration time between the lanthanum and scandium planes practically does not depend on the direction, and the proportion of transitions to the scandium plane is much greater than from it. Consequently, this jump is more advantageous for a proton than moving in the lanthanum plane, so it prefers to move in the direction of the scandium plane. At the same time, proton movement in the scandium plane and exit from it are equally probable (the proportions of jumps of these types are the same), but for movement in the Sc plane, a proton needs to overcome a more significant potential barrier than in order to exit it. Therefore, the time of the jump in the scandium plane is longer.

According to the Arrhenius law (taking into account the Nernst–Einstein equation), the dependence of proton conductivity σ on the inverse temperature can be represented as a linear dependence $\ln\sigma(1/T)$. To calculate the average activation energy for proton movement, the data presented in Figs. 7a and 7b were used; i.e., the average activation energy was determined taking into account the contribution of each type of proton jump. Equation (1)

$$\ln\sigma(1000/T) = 0.028 - 7.328(1000/T), \qquad (1)$$

reflecting the calculated temperature dependence of the proton conductivity in $LaScO_3$ perovskite, is shown in Fig. 8. A similar dependence was determined for oxygen ions, holes, and protons diffusing in calcium-doped crystalline perovskite $La_{0.9}Ca_{0.1}ScO_{3-\delta}$ in a narrow range (from 626 to 867 K) by electrochemical impedance method [18]. Satisfactory agreement of the slopes of the $\ln\sigma(1000/T)$ dependences for $La_{0.9}Ca_{0.1}ScO_{3-\delta}$ and $LaScO_3$ was obtained. Ceramics $La_{0.9}Ca_{0.1}ScO_{3-\delta}$ is one of the most highly conductive solid ion conductors ($\sigma = 1.8 \times 10^{-3}$ S/cm at $T = 867$ K and $\sigma = 5.8 \times 10^{-5}$ S/cm at $T = 626$ K) [18]. Note that the ionic conductivity level of a traditional liquid electrolyte, as a rule, is approximately 10^{-2} S/cm [19]. Due to doping with divalent Ca, oxygen vacancies are created in perovskite, which increases the overall conductivity. The dependence $\ln\sigma(1000/T)$ for $La_{0.9}Ca_{0.1}ScO_{3-\delta}$ is slightly higher than the corresponding dependence for $LaScO_3$.

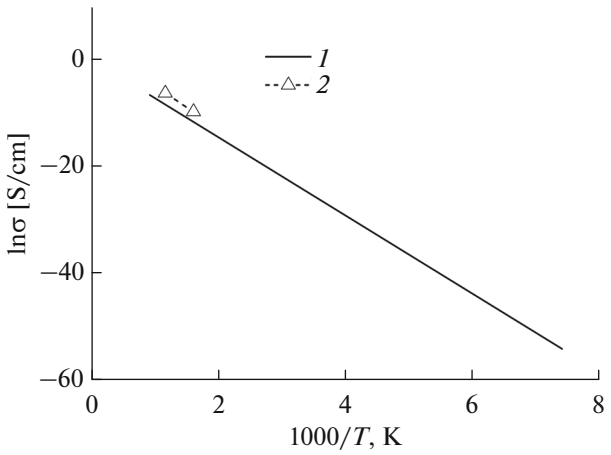

Fig. 8. (*1*) Dependence of lnσ on parameter $1000/T$ for constant weighted average activation energy $E_a = 1.255$ eV for proton motion along defect-free perovskite $LaScO_3$, obtained by *ab initio* MD. (*2*) Values of similar characteristic for $La_{0.9}Ca_{0.1}ScO_{3-\delta}$, obtained by electrochemical impedance method [18].

CONCLUSIONS

Proton conductivity in defect-free perovskite $LaScO_3$ has been investigated. Understanding the nature of proton conductivity in a defect-free material, which occupies at least 80% even in doped and oxygen-rich metal oxide crystals with a perovskite structure, is important for further improvement of environmentally friendly energy devices. In this study, the behavior of a proton in a $LaScO_3$ crystal was investigated depending on the initial location and speed, as well as the external electric field and temperature. The intermittent nature of proton diffusion in the studied perovskite has been found and four types of jumps determined by the structural features of this compound have been identified. A number of facts support the polaron nature of proton migration in $LaScO_3$ perovskite. In particular, this was confirmed by the fact that the trajectory of a proton is determined to a greater extent by its immediate environment and the temperature of the system than by the external electric field.

The average execution time of all types of proton jumps was from 32 to 47 fs, and the activation energy for proton movement varied in the range $0.95 \le E_a \le 1.75$ eV. The difference in frequencies of different types of jumps could be 2.3 times. Proton migration in solid defect-free perovskite $LaScO_3$ was characterized by equation (1).

Proton transfer was facilitated by cooperative processes, such as lattice vibrations. In perovskites of the ABO_3 type, the level of proton conductivity depends on the nature of the atoms in this compound. Usually, proton conductivity increases with a decrease in the electronegativity of elements A and B. An increase in proton conductivity due to doping of perovskite has fundamental limitations. First, the formation of an oxygen vacancy is associated with the breaking of the oxygen–metal (O–M) bond, which requires a certain amount of energy. Secondly, the formation of an electrically neutral vacancy is accompanied by the reduction of neighboring cations [20] and, consequently, produces a change in chemical energy. Thirdly, with an excessive amount of oxygen vacancies, the stability of the compound containing them may be violated [21]. Thus, only a limited number of oxygen vacancies can be created in ABO_3-type perovskite.

Despite considerable efforts to find satisfactory solid electrolytes, the problem of achieving favorable ionic conductivity remains unsolved. One of the main challenges is the lack of systematic knowledge about

the mechanisms of ion transport, which could contribute to an increase in ionic conductivity. In other words, a scientific understanding of these mechanisms is considered as a critical element for the productive use of solid electrolytes. The generally accepted fundamental physical picture of ion migration in ion conductors is the idea of the abrupt nature of their movement from one occupied position to another [22]. There are many reviews suggesting various mechanisms of ion transport in solid electrolytes [23, 24]. However, a universal scheme for increasing ionic conductivity has not yet been developed.

The jumplike motion of a proton through a solid electrolyte is a thermally controlled process. To create rapid proton diffusion, defective regulation is most often used, since it is convenient and effective. However, an increase in proton conductivity by doping is limited by the maximum concentration of defects at which it is possible to maintain the existence of a crystal structure. In the case of several types of charge carriers (i.e., different ions), the use of a coordinated migration mechanism in solid electrolytes can also significantly increase ionic conductivity. The close interaction of the lattice sceleton with mobile ions slows down the movement of ions and reduces ionic conductivity.

Thus, the main concepts of increasing ionic (and in particular proton) conductivity are to provide rapid diffusion for mobile ions and reduce the resistance of the potential field surrounding them. A significant improvement in the characteristics of clean energy devices is possible due not only to the increased influence of oxygen vacancies, but also to improvement of the proton migration mechanism along a perfect perovskite.

FUNDING

The study was partially supported by the Government of the Russian Federation, state task no. 075-03-2022-011 of 14.01.2022 (FEUZ-2020-0037); and part of the study was carried out within the scientific topic of the Institute of High-Temperature Electrochemistry, Ural Branch, Russian Academy of Sciences, project no. FUME-2022-0005, registration no. 122020100205-5.

CONFLICT OF INTEREST

The author of this work declares that he has no conflicts of interest.

REFERENCES

1. Zhang, W. and Hu, Y.H., *Energy Sci. Eng.*, 2021, vol. 9, p. 984.
2. Smirnov, B.M., *High Temp.*, 2021, vol. 59, p. 207.
3. Wang, Q., Wei, H.-H., and Xu, Q., *Sustainability*, 2018, vol. 10, p. 2395.
4. Khaskhachikh, V.V., Larina, O.M., Sychev, G.A., Gerasimov, G.Ya., and Zaichenko, V.M., *High Temp.*, 2021, vol. 59, no. 3, p. 373.
5. Kreuer, K.D., Paddison, S.J., Spohr, E., and Schuster, M., *Chem. Rev.*, 2004, vol. 104, p. 4637.
6. Gorelov, V.P. and Stroeva, A.Yu., *Russ. J. Electrochem.*, 2012, vol. 48, no. 10, p. 949.
7. Caramanico, N., Di Florio, G., Baratto, M.C., Cigolotti, V., Basosi, R., and Busi, E., *Energies*, 2021, vol. 14, p. 5847.
8. Inaguma, Y., Liquan, C., Itoh, M., and Nakamura, T., *Solid State Commun.*, 1993, vol. 86, p. 689.
9. Birke, P., Scharner, S., Huggins, R.A., and Weppner, W., *J. Electrochem. Soc.*, 1997, vol. 144, p. L167.
10. Stramare, S., Thangadura, V., and Weppner, W., *Chem. Mater.*, 2003, vol. 15, p. 3974.
11. Zhao, G., Suzuki, K., Hirayama, M., and Kanno, R., *Molecules*, 2021, vol. 26, p. 299.
12. Hellstrom, E.E. and Van Gool, W., *Solid State Ionics*, 1981, vol. 2, p. 59.
13. Hui, W., Chao, L., Lu, H., et al., *Science*, 2021, vol. 371, no. 6536, p. 1359.
14. Fang, Z., Jia, L., Yan, N., et al., *InfoMat*, 2022, vol. 4, no. 6, p. e12307.
15. Perdew, J.P., Burke, K., and Ernzerhof, M., *Phys. Rev. Lett.*, 1996, vol. 77, p. 3865.
16. Siesta-pro/siesta-pseudos-and-basis-database. http://www.simuneatomistics.com/siesta-pro/siesta-pseudos-and-basis-database/.
17. Monkhorst, H.J. and Pack, J.D., *Phys. Rev. B*, 1976, vol. 13, p. 5188.
18. Belova, K., Egorova, A., Pachina, S., and Animits, I., *Appl. Sci.*, 2022, vol. 12, p. 1181.
19. Wang, C., Xu, B.B., Zhang, X., Sun, W., Chen, J., Pan, H., Yan, M., and Jiang, Y., *Small*, 2022, vol. 18, no. 43, p. 2107064.
20. Pavone, M., Munoz-Garcia, A.B., Ritzmann, A.M., and Carter, E.A., *J. Phys. Chem.*, 2014, vol. 118, p. 13346.
21. Park, M.H., Lee, D.H., Yang, K., Park, J.-Y., Yu, G.T., Park, H.W., Materano, M., et al., *J. Mater. Chem.*, 2020, vol. 8, p. 10526.
22. Girifalco, L.A., *Statistical Physics of Materials*, New York: Wiley, 1973.
23. Zhang, B., Tan, R., Yang, L., et al., *Energy Storage Mater.*, 2018, vol. 10, p. 139.
24. Yang, H. and Wu, N., *Energy Sci. Eng.*, 2022, vol. 10, no. 5, p. 1643.

Translated by E. Puchkov